



# Ultrasonic inspection of lithium-ion pouch cells subjected to localized thermal abuse

Tyler M. McGee<sup>a</sup>, Barrett Neath<sup>a,b</sup>, Sam Matthews<sup>a</sup>, Ofodike A. Ezekoye<sup>a</sup>,  
Michael R. Haberman<sup>a,b,\*</sup>

<sup>a</sup> Walker Department of Mechanical Engineering, The University of Texas at Austin, Austin, TX, USA

<sup>b</sup> Applied Research Laboratories, The University of Texas at Austin, Austin, TX, USA

## HIGHLIGHTS

- Ultrasonic inspection of lithium-ion batteries subjected to localized thermal abuse.
- Use of multiple ultrasonic frequency-path pairs improve sensitivity to damage.
- Cell properties change as a result of temperature and induced chemical reactions.
- Ultrasonic metrics indicate thermal damage in advance of conventional techniques.
- Ultrasonic monitoring provides an early warning of thermal runaway.

## ARTICLE INFO

### Keywords:

Lithium-ion  
Ultrasonic monitoring  
Damage detection  
Battery safety  
Thermal runaway  
Nickel Manganese Cobalt

## ABSTRACT

Safety concerns associated with thermal runaway (TR) in lithium-ion cells have limited their adoption in high-power applications such as battery electric vehicles or energy storage systems. In practice, cells are more likely to encounter localized heating than total volume heating, so detecting and preventing TR in this thermal loading environment remains critically important. In this work, we employ ultrasonic inspection (US) to probe NMC lithium-ion cells subjected to localized, thermal loading to illustrate the utility of ultrasonic methods for TR detection. The method employs US Gaussian pulses with two different center frequencies propagating along two different paths to gain additional knowledge of the internal state of a mechanically-confined, thermally-loaded pouch cell during localized heating between 200°C and 450°C in different iterations of the test. The time of flight shift (TOFS) and signal amplitude (SA) are used to indicate thermal loading. For a given frequency-path pair the TOFS and SA trends under different levels of thermal loading are consistent. Damage indicators are developed using the US characteristics to give a time-before-TR warning. We demonstrate that through the use of multiple frequency-path pairs and ultrasonic metrics, US measurements can detect an impending battery failure up to twenty-five minutes in advance of TR.

## 1. Motivation and background

Lithium-ion batteries (LIBs) have been used extensively in consumer electronics since 1991, when Sony created the first commercial rechargeable LIB. Consumer electronics applications include phones, laptops, and power tools. However global energy trends demand robust solutions for high-power systems, such as electric vehicles, and intermittent systems, such as energy storage systems for renewable sources such as solar and wind power. These applications differ from traditional consumer electronics applications in a few critical ways. First, these LIB systems require hundreds to thousands of cells connected in battery packs to achieve higher power and higher capacity. The sheer increase in number of cells per application raises the risk of a thermal runaway

event. Additionally, the introduction of LIBs into electric vehicles raises the risk of mechanical, thermal, and even electrical abuse as electric vehicles require fast charging and discharging to attain the desired vehicle performance. The likelihood of failure and the increased significance of damage from applications requiring higher capacity and power delivery motivates researchers to improve battery management systems (BMS) in order to ensure battery safety in real time. The present work explores the viability of using ultrasonic inspection (US) to determine battery safety when a cell is subjected to localized, high-temperature thermal abuse.

State-of the art BMS use open-circuit voltage (OCV) and current measurements for state estimation, leveraging the relationship between

\* Corresponding author at: Walker Department of Mechanical Engineering, The University of Texas at Austin, Austin, TX, USA.

E-mail addresses: [tm34485@utexas.edu](mailto:tm34485@utexas.edu) (T.M. McGee), [bneath@utexas.edu](mailto:bneath@utexas.edu) (B. Neath), [smatthews95@gmail.com](mailto:smatthews95@gmail.com) (S. Matthews), [dezekoye@mail.utexas.edu](mailto:dezekoye@mail.utexas.edu) (O.A. Ezekoye), [haberman@utexas.edu](mailto:haberman@utexas.edu) (M.R. Haberman).

<https://doi.org/10.1016/j.jpowsour.2023.233542>

Received 8 January 2023; Received in revised form 29 July 2023; Accepted 20 August 2023

Available online 2 September 2023

0378-7753/© 2023 Elsevier B.V. All rights reserved.

OCV and SOC [1]. Thermocouples are placed on the exterior of cells to detect thermal abuse and to ensure all cells in the pack are subjected to the same operating temperature. Externally-placed thermocouples fail to accurately detect the internal temperature of LIBS [2]. US monitoring allows for sensor placement away from the active leads of the cell and may be able to provide information on the internal temperature of cells by correlating changes in the ultrasonic signal resulting from the thermally-induced changes of the mechanical properties of internal cell components. The viability of ultrasonic detection for LIBs has been established starting in 2014. Sood et al. took ultrasonic data and X-ray images of a cell before and after aging to 75% SOH [3]. Other early studies have shown the utility of ultrasonic inspection for SOC determination [4–14]. Early work on this topic has shown that there is a correlation between the shift in the time of flight (TOF) and SOC which allows TOF to be used as an indicator of SOC [6,8,9,12–14]. Following these early studies, other groups have employed ultrasonic inspection to solid-state batteries, silicon anode batteries, and lithium-ion capacitors to monitor dendrite formation, state estimation, and overcharge and under-discharge, respectively [15–18]. Other studies have shown that ultrasonic inspection can detect mechanical damage occurring within a LIB cell. Bommier et al. intentionally induced lithium plating in lithium-ion cells and correlated the change in ToF with degree of lithium plating [19]. Similarly, Chang and Steingart induced lithium plating via fast charging and showed a correlation between attenuation and lithium plating [20].

Recent research has investigated US as a means to detect high-temperature thermal abuse of lithium-ion batteries. This work can be divided into two categories: (i) moderate heating within prescribed limits and (ii) heating to failure. Importantly, failure can be defined either as when the cell first ruptures and becomes inoperable or when the cell catastrophically fails in a thermal runaway (TR) event. Many groups have used moderate heating between 30°C and 45°C to accelerate aging in order to study the correlation of ultrasonic signal features such as global decreases in TOF shift and an increasing range of SA with SOC as cells age [9,11,21]. Wu et al. used 45°C moderate heating to accelerate damage evolution of overcharge [22] and Pham et al. heated cells to failure, although the temperatures and whether the cells reached thermal runaway is not reported [23]. Chang et al. cycled cells in temperature-controlled incubators from 0°C to 60°C while taking ultrasonic measurements [21]. Similarly, Popp et al. measured TOF while a cell was slowly heated from 5°C to 45°C and found that the TOF increased with temperature following a cubic relationship [6]. Ke et al. also found that the TOF increased as the cell was heated from room temperature to 40°C [4]. Owen et al. heated cells in a temperature chamber in a range of temperatures from –10°C to 60°C and found a linear increase in TOF [5]. In a different study, Appleberry et al. overcharged cells to failure using both constant-current and constant-voltage overcharging at both room temperature and 65°C finding that SA increases and the TOF decreases beyond 3.5 standard deviations of their normal cycling values at various points during overcharge [24]. The study by Bommier et al. investigating lithium plating by cycling batteries at low temperatures also provided data for anodes cycled at temperatures as high as 60°C to show that more lithium plating occurs at low temperatures [19]. Zappen et al. heat cells uniformly in an adiabatic calorimeter to both thermal runaway and venting in separate iterations of their experiment, although acoustic data are only taken when the cells were heated to 110°C, which did not induce venting or TR [25]. Kirchev et al. heat cylindrical, prismatic cells with cathode chemistry NMC 811 and anode chemistry G-SiO<sub>x</sub> at 0%, 50%, 100%, and 120.3% SOC to 160°C in an adiabatic calorimeter which did induce TR for cells at 100% and 120.3% SOC. They found that SA decreased nearly linearly with temperature [26]. Previous research has studied the effects of thermal loading by applying total volume heating to the cells. The use of total volume heating does not clearly answer the question about whether the ultrasonic transducers need to be co-located with the region of elevated cell temperature

for damage detection. Additionally, it is unlikely that a cell would be uniformly heated to thermal runaway *in situ*. Alternatively, local temperature gradients may form near the current collector tabs and near locations of high internal resistance during normal cycling [27–29]. Localized heating to thermal runaway has also been used as an experimental approximation of the effect of an internal short circuit in the cell, which can cause localized heating to temperatures as high as 500°C [30]. Localized heating has also been used to simulate the propagation of thermal runaway from an adjacent cell in a planar array [31,32].

This work investigates the use of ultrasonic signal metrics as a means of detecting the conditions leading to TR caused by local heating. This is achieved using localized heating of LIB pouch cells from 200–450°C in 50°C increments when subjected to mechanical confinement and instrumented with three ultrasonic transducers to enable pitch-catch measurements along two transmission paths, through-thickness and guided waves, using Gaussian pulse excitation with two different center frequencies. Changes in SA and TOF of the ultrasonic signals are monitored as a function of heater temperature and used as metrics to indicate departure from normal cell conditions. We also introduce a multiscale model of the pouch cell using a continuum approximation to better understand propagating elastic wave modes within the cell at the measurement frequencies. The multiscale model consists of an analytical layered-medium model to estimate the transversely anisotropic effective stiffness of the pouch cell which is then used as an input to a time-domain finite element model of the LIB cells including the finite-sized transducers. To our knowledge, this is the first ultrasonic study of localized, high-temperature abuse of LIBs with temperatures greater than 160°C. We correlate changes in key ultrasonic signal parameters with temperature, pressure, and electrical data to understand the mechanical changes occurring within the cells and to create damage indicators which warn of an impending thermal runaway event. The results of this work expand the applicability of US inspection of thermal abuse of lithium ion cells by showing that US detection is agnostic to transducer location relative to the heat source. The structure of this article follows. Section 2 describes the experimental setup, parameters of data acquisition, and measurement procedure. This section includes specifications for key experimental components including the transducers and batteries. The results from the experiments are given in Section 3, which also includes definitions for ultrasonic-based metrics to warn of localized heating. Conclusions are given in Section 4.

## 2. Experimental setup and procedure

The experimental setup is comprised of three systems: the US system, the battery cycler, and the mechanical clamping rig. The cells are placed in the mechanical clamping rig to provide realistic pressure-loading approximating battery pack confinement and to locate the barrel heater and transducers. Before applying heat, the cells are cycled while measurements are made of US signals, local temperatures, cell pressure, and the current and voltage at the cell terminals. The cell is then disconnected from the battery cycler for the heating portion of the test where we record US signals, local temperature, cell pressure, and cell voltage.

The cells used in this work are 10 Ah Nickel Manganese Cobalt (NMC) 532/graphite pouch cells with a nominal voltage of 3.70 V and a maximum charge cut-off voltage of 4.20 V. The dimensions ( $L \times W \times H$ ) of the cell are approximately 162 mm  $\times$  60 mm  $\times$  11 mm, with Al and Cu current collector tabs extending beyond this rectangular envelope at one end of the cell. The proprietary electrolyte constitutes 10%–20% of the total cell weight. The specifications provided by the vendor, AA Portable Power Corp., state an operating temperature range of 0–45°C during charge and 0–60°C during discharge.

## 2.1. Ultrasonic system

The ultrasonic system consists of three cylindrical disk transducers epoxied to the pouch cell, the excitation electronics, and the ultrasonic data acquisition system (DAQ). The transducers are low-cost piezoelectric ceramic (modified PZT-4) disks acquired from Steiner & Martins, Inc. (model SMD10T2R111) and are used to generate and receive ultrasonic signals. They have an outer diameter of 10.0 mm, a thickness of 2.0 mm, and are polarized in the through-thickness (longitudinal) direction. The transducers have two resonance frequencies, one associated with a radial resonance and another associated with a thickness resonance. The thickness-mode has a resonance frequency of 1 MHz, and the radial-mode has a resonance frequency of 220 kHz, allowing a single transducer to generate high amplitude pulses at two well-separated center frequencies. Three transducers are epoxied to the surface of the cell using Permatex 84102 high-temperature epoxy in a pitch-catch configuration, as shown in Fig. 2. Epoxy is used in lieu of gel couplant for more robust and repeatable adhesion to the cell casing, ensuring high performance at elevated temperatures up to 260°C, and improved generation and reception of acoustic energy between the transducers and the pouch cell. It will be shown that the temperature at the transducer locations does not exceed 200°C even with heater temperatures up to 450 degC. Two propagation paths are used in this work: through-thickness and guided-wave transmission. The locations of the transducers are chosen to avoid interaction with the current collector tabs and edge effects caused by the side walls of the casing, which we have verified in prior work [33]. The dual-resonance behavior of the transducers allow for the generation and reception of two signals as the state of the battery changes during the experiment. Specifically, two Gaussian-modulated cosine voltage signals, each centered on the resonance frequencies of the transmitting transducer, are provided sequentially in time such that each acquisition captures four waveforms corresponding to the following frequency-path pairs: 215 kHz-Through, 215 kHz-Guided, 1 MHz-Through, and 1 MHz-Guided. As the cell is heated, the ultrasonic data acquisition system records acoustic waveforms every 500 ms.

The ultrasonic system consists of a National Instruments PXIe-1078 9-slot chassis with three modules for signal generation and data collection. A custom LabVIEW VI on an external PC is used to control signal generation and acquisition. A five-cycle Gaussian-modulated cosine voltage pulse is generated with the National Instruments PXIe-5413 Waveform Generator based on the following equation where  $V_0$  is the maximum amplitude of the pulse,  $t_0$  is the time corresponding to the center of the pulse, and  $\omega_0$  is the angular center-frequency of the pulse:

$$V(t) = V_0 \cos [\omega_0 (t - t_0)] \exp \left[ -\frac{(t - t_0)^2}{2T^2} \right] \quad (1)$$

The waveform is amplified with a Krohn-Hite Model 7500 Wideband Power Amplifier before being sent to the transmitting transducer. The receiving transducers generate voltage signals proportional to the elastic wave motion at the measurement location which is acquired using a PXIe-6386 Multifunction I/O Module through a National Instruments BNC-2110 Terminal Block. The received signals are filtered with a Krohn-Hite Model 3988 Dual Channel High-Pass Filter with a high-pass frequency of 100 kHz and averaged across five acquisitions to reduce zero-mean noise. A schematic diagram of the experimental system which shows device connectivity and signal flow is provided in Fig. 1.

## 2.2. Mechanical clamping and heating system

In order to replicate realistic pressure loading, the pouch cell is compressed in a multi-functional mechanical confinement rig constructed from three aluminum plates held together using nuts and bolts, similar to refs [34,35]. A TE Connectivity FX 1901 load cell is placed between the bottom two plates to continuously measure force as the cell expands and contracts during electrical and thermal loading. In order to induce

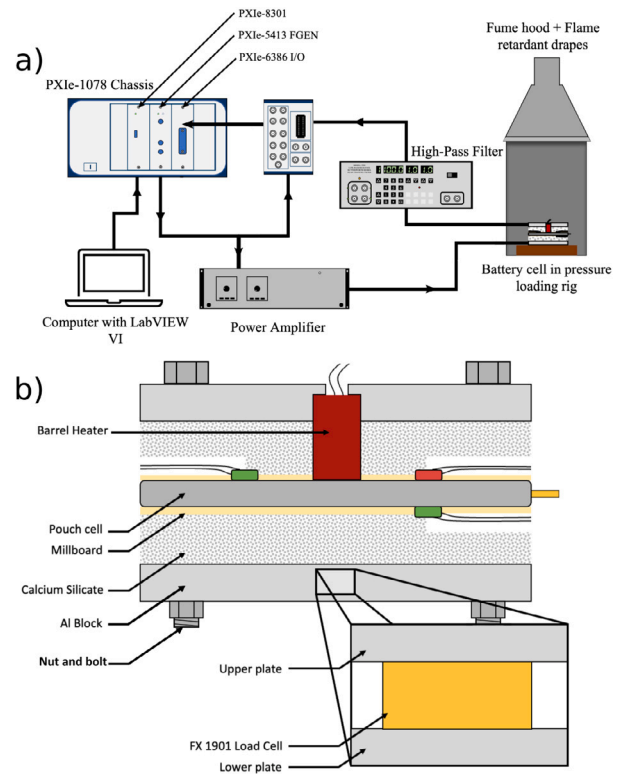
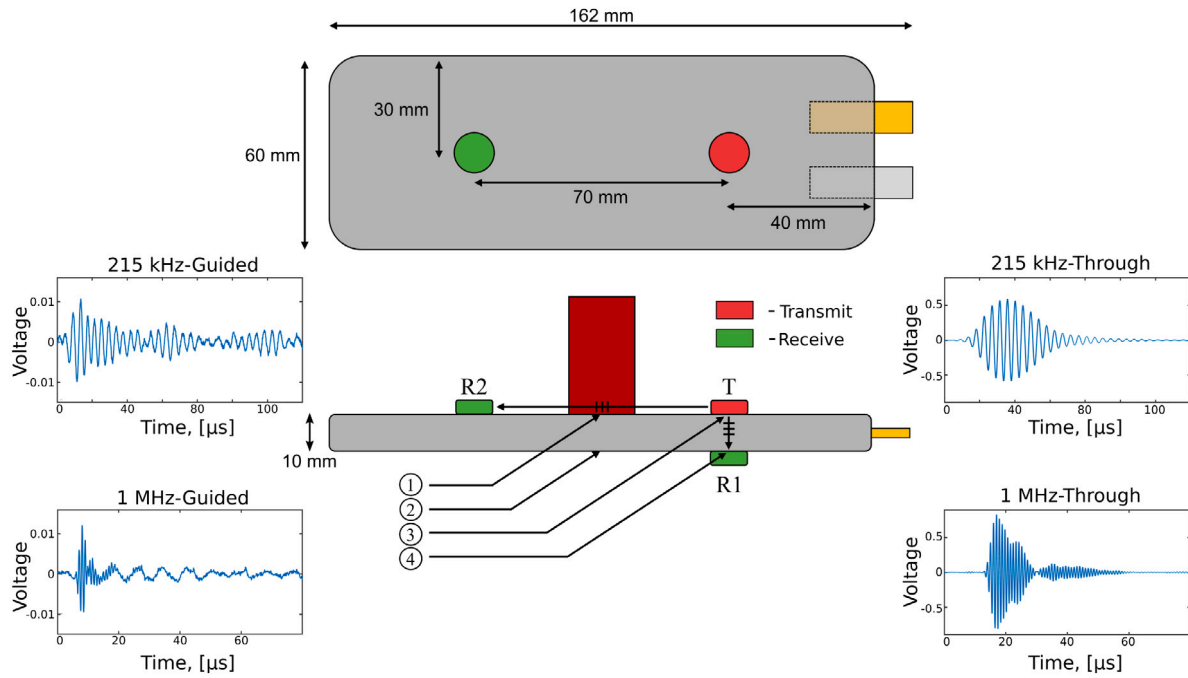


Fig. 1. (a) Signal chain of the ultrasonic measurement system. The input signal is generated via a custom LabView VI and amplified before being sent to the transmitting transducer. The signal is high-pass filtered and averaged before being recorded. (b) The mechanical clamping rig locates the cell, transducers, and barrel heater. A pressure of 30 kPa is applied via nuts and bolts and recorded with a load cell between the bottom two aluminum plates prior to pre-conditioning and heating.

TR via localized heating, a 19 mm barrel heater is placed in contact with the top face of the cell and is controlled by an Omega CN8241-F1-RSP4 PID temperature controller. The pouch cell is sandwiched between two sheets of millboard and two calcium silicate blocks in order to provide thermal isolation between the pressure rig and the pouch cell. The millboard and calcium silicate blocks are machined to accommodate the transducers and to maintain even pressure across the entire face of the cell. As indicated in Fig. 2, four K-type thermocouples are placed on the surface of the cell in order to measure the temperature at the heater, on the opposite side of the cell, at the heater-side transducer, and at the far-side transducer. As the cell is heated, the Graphtec midi LOGGER GL840 records pressure, temperature, and cell voltage every 100 ms.

## 2.3. Electrochemical cycling

Before the cells undergo thermal abuse testing, they are cycled in the pressure rig using an Arbin LBT21084 8-channel battery cycler. These cycles serve to ensure that the cells cycle normally at their rated capacity, and the US data taken during these cycles is used to ensure that the epoxied transducers are effectively bonded to the cell. For example, if the received signal's amplitude during pre-heating cycling is very low compared to previous studies or if the amplitude suddenly drops before the application of heat, this suggests that one or more of the US transducers is not properly bonded to the cell which should be remedied prior to heating. The pouch cell is loaded to an initial pressure of 30 kPa, and the cell is cycled using a low-impact CC-CV charging protocol, a single cycle of which is outlined in Table 1. The final steps in the charging protocol before any heat is applied are a constant current charging and a constant voltage charging to



**Fig. 2.** Schematic showing the cell dimensions and locations of the three transducers and four thermocouples. The circled numbers one through four indicate the thermocouple locations. Exciting the transmitting transducer with two signals with different center frequencies and acquiring signals with two receiving transducers provides data for four frequency-path pairs. The through-thickness path data is the signal sent from the transmitting transducer “T” to the receiving transducer labeled “R1”. The guided-wave path data is the signal sent from the transmitting transducer “T” to the receiving transducer labeled “R2”. The figure shows representative waveforms for each frequency-path pair where we note the amplitude of the guided-wave signal is an order of magnitude smaller than the through-thickness signal. Regardless, both signal paths provide reliable information about heat-induced changes within a LIB cell.

**Table 1**  
Single low-impact CC-CV charge cycle protocol used for pre-conditioning cycles.

Step	Limit
Rest	1 min
0.5C Constant-Current Charge	4.20 V
4.20 V Constant-Voltage Charge	0.05 C Rate
Rest	5 min
0.5C Constant-Current Discharge	2.75 V
Rest	10 min

100% SOC. During cycling, the Arbin software records voltage, current, capacity (Ah), energy passed (Wh), and the time rate-of-change of cell voltage [V/s] at one minute intervals; a Graphtec midi LOGGER GL840 records pressure and temperature data every second; and the LabVIEW VI records acoustic waveform snapshots every minute with a sampling frequency of 14.29 MS/s. Care is taken such that each data acquisition hardware is started at the same time to assure time-synchronization.

#### 2.4. Heating protocol

Cells were heated to different hold temperatures ranging from 200°C and 450°C at 50°C increments using a prescribed temperature ramp rate of 43°C/min for all set temperatures. This ramp rate is taken from the rate necessary to heat from room temperature to 450°C in ten minutes. After this ramp time, the heater is held constant at a prescribed hold temperature until TR or for two hours if TR is not initiated. After this applied heating, the heater is turned off and the cell is allowed to cool for an additional two hours. Ultrasonic data is taken throughout both heating and cooling portions of the test.

#### 2.5. Modeling methods

A finite element model was created using COMSOL Multiphysics to understand the ultrasonic fields being used to interrogate the cell when

excited using the Gaussian pulse waveforms described in Section 2.1. Understanding the mode of propagation is important when interpreting what kinds of mechanical changes are being observed within the cell. To simplify the model, only the anode, cathode, and separator were considered. Estimates of the elastic moduli of the anode and cathode materials were taken from Qi et al. [36] and the moduli of the polypropylene separator was found in Vgenopoulos et al. [37]. Due to a lack of available data, the stiffness tensor for LiCoO<sub>2</sub> was used in place of NMC. While it is well understood that LiCoO<sub>2</sub> has lower electrochemical stability than NMC due to the release of oxygen at full discharge, the stiffness tensors of LiCoO<sub>2</sub> and NMC are assumed to be approximately equal [38]. The effective anisotropic stiffness of the layered structure of the cell was modeled using a homogenized material model, assuming the material to be transversely isotropic and using simplifying assumptions of constant stress or constant strain as detailed in Appendix. These assumptions are valid as a leading order approximation for layered materials whose material properties are constant in a given layer, but vary in the direction perpendicular to the layers [39]. Individual stiffness tensor components were averaged either with Reuss or Voigt averaging rule-of-mixtures approximations for each element of the effective stiffness tensor to model the heterogeneous material as a homogenized material with transversely isotropic stiffness. A more detailed explanation of the homogenization model and COMSOL model parameters is included in Appendix.

The cell geometry and transducers are modeled exactly as they are in the experiments. Three transducers are used, one as the transmitter and two as receivers in the locations indicated Fig. 2. One is located on the opposite face of the pouch cell as the transmitter to capture the through-thickness signal and the other is on the same surface as the transmitter 70 mm apart to capture the guided-wave signal. Gaussian modulated cosines with two center frequencies equal to the two resonance frequencies of the transducers, 215 kHz and 1 MHz, are used to excite the transmitting transducer. The pressure field after some time is plotted for each of the two different excitation signals in Fig. 3(a) and 3(b). From this simulation, we observe that the pressure



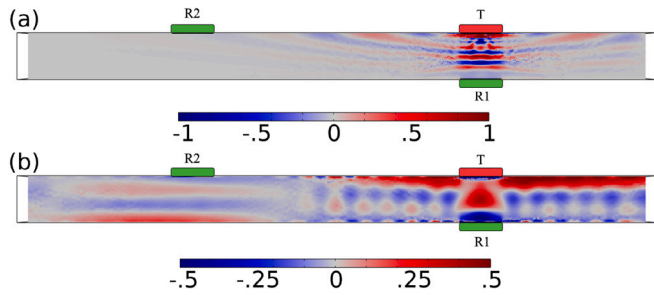


**Fig. 3.** Finite element simulation of the ultrasonic wave fields for the two different excitation waveforms. The surface color represents the pressure field. (a) 1 MHz center-frequency excitation which excites the thickness-mode resonance of the transmitting transducer. The pressure field is localized between the transmitter, “T”, and receiving transducer, “R1”. This is the through-thickness ultrasonic path. (b) 215 kHz center-frequency excitation which excites the radial resonance of the transmitting transducer. The pressure field consists of a through-thickness standing wave pattern that propagates from the transmitter, “T” to the receiving transducer “R2”. This is a Lamb-wave like propagating mode, which we label as the guided-wave path.

field produced by the 215 kHz input resembles a Lamb mode [40], which have recently been exploited by Jie et al. to study SOC in lithium-ion pouch cells using Biot theory and a transfer matrix approach [41]. A standing pressure field, which is influenced by both the top and bottom cell surfaces, develops within the cell thickness and propagates in the plane of the cell. The ultrasonic signals received from a 215 kHz center-frequency excitation will provide information about material property changes, volumetric damage, and/or changes in boundary conditions anywhere in the cell between the transmitter and receiver labeled “R2” in Fig. 3(b). On the other hand, the 1 MHz signal travels as a collimated ultrasonic beam from the transmitting to the receiving transducer labeled “R1” in Fig. 3(a). This shorter wavelength, direct path will be more impacted by delamination or gas formation in the transmission path, as these damage conditions present large impedance contrasts which reflect and absorb the transmitted ultrasonic wave.

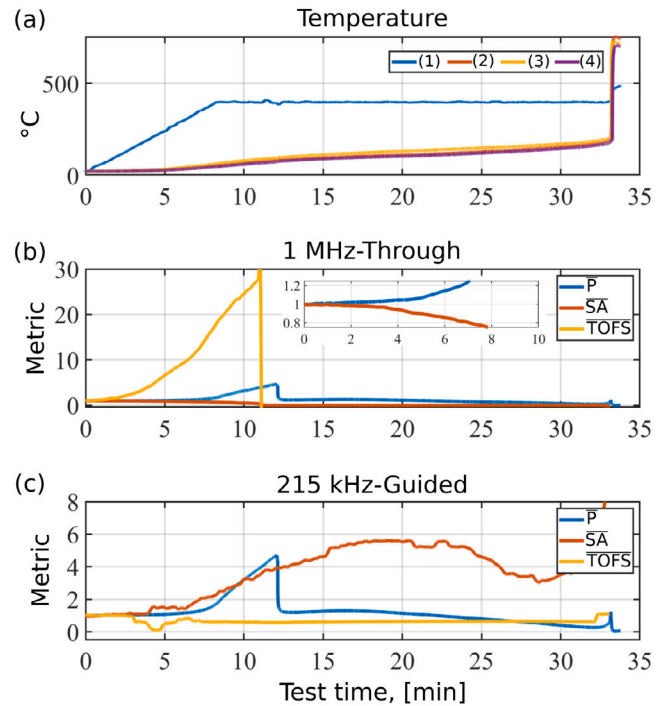
### 3. Results and discussion

Fig. 2 shows a representative received signal for each frequency-path pair. For each center-frequency of excitation, the amplitude of the guided path is much lower than that of the through-thickness path. This is due to the fact that, though the transducers resonate at both 215 kHz and 1 MHz, the transducer geometry is not optimized to launch and sense guided waves of this wavelength. This will be addressed in future work. For the 1 MHz input frequency the received signal of the guided path is very low amplitude and just above the noise floor. Therefore, no further analysis on the data for the 1 MHz guided wave path is conducted in the present work. While the 215 kHz, through-thickness path data is well above the noise floor, the guided wave signal at this frequency is of greater interest given the Lamb-like mode excited by a 215 kHz radial resonance of the source transducer that ensoufies the entire volume of the LIB between transmitter and receiver.

In this work, the ultrasonic signal characteristics used are the signal amplitude (SA) and time of flight shift (TOFS), which are defined here. The overall SA metric used here employs the absolute value of each data point of a received signal and sums between initial and final times,  $t_i$  and  $t_f$ , respectively, of the received signal using

$$SA = \int_{t_i}^{t_f} |f(t)| dt. \quad (2)$$

To increase the resolution of the TOFS, the raw signal is first upsampled using MATLAB’s interp function with a factor of ten. The TOFS is calculated by cross-correlating the envelope of the upsampled signal at each acquisition with the envelope of the upsampled signal prior to thermal loading. The cross-correlation approach takes into account



**Fig. 4.** Representative temperature, pressure (P), signal amplitude (SA), and time-of-flight shift (TOFS) data as a function of test time. The data shown here is for 400°C heating. (a) Temperature from thermocouples located at positions indicated in Fig. 2. (b) and (c) provide the normalized pressure,  $\bar{P}$ , normalized SA,  $\bar{SA}$ , and normalized TOFS,  $\bar{TOFS}$ . The normalization of dataset,  $X(t)$  is defined as  $\bar{X}(t) = X(t)/X(0)$ , where  $X(t)$  represents  $P(t)$ ,  $SA(t)$ , or  $TOFS(t)$ . The inset image in (b) is used to show the decrease in SA which precedes cell venting.

delays inherent to the signal chain to provide an estimate of the change in the TOF for the pulse. The TOFS therefore determines a change in the group velocity of the wave packet between the pristine cell and the cell after electrical cycling and localized heating. Upsampling is used to increase the resolution the TOFS estimate, as the position of the maximum of a cross-correlation of a signal is limited by the sampling frequency of the data acquisition hardware. Upsampling the signal increases the TOFS resolution and smooths out the computed TOFS curves.

Appropriate context is given to the ultrasonic data by simultaneously monitoring cell temperature, pressure, and open circuit voltage. Fig. 4 includes the SA, TOFS, and temperature and pressure data for the 400°C test. The SA, TOFS, and pressure data has been normalized by the value of the metric at when heating begins, which we define as  $t = 0$ . In the 400°C hold temperature test shown here the cell vents at 12.7 min. Initial cell venting occurs when the pouch cell casing opens due to the internal pressure associated with electrolyte evaporation and is evident from the sudden decrease in cell pressure in the  $\bar{P}$  data shown in both Figs. 4(b) and 4(c). The pressure accumulates again until major venting occurs at 20.3 min. This major venting is associated with gas generation from component decomposition on the route to TR. The cell finally goes into TR after 38.9 min. Importantly the cell voltage remains fairly agnostic to increases in temperature and cell pressure, rendering it a poor indicator of localized thermal abuse. At the 35th minute the cell voltage has dropped from 4.164 V to 4.080 V. A similarly low reduction in cell voltage is observed in all tests. It will be shown that the 2% decrease in cell voltage is very small compared to the percent-change in ultrasonic signals characteristics. As such cell voltage will not be reported with SA, TOFS, temperature, and pressure in the remainder of this work.

Data for the normalized pressure, SA, and TOFS for the 1 MHz-Through and 215 kHz-Guided frequency-path pairs are plotted from

the 400°C test in Fig. 4. For the 1 MHz-Through data, the SA decreases with thermal loading, while the TOFS increases. A different trend is observed in the 215 kHz-Guided data. The SA tends to increase with thermal loading, while the TOFS data is noisy and unreliable due to low signal amplitude levels. When the cell first vents the 1 MHz-Through SA drops to the noise floor, whereas the increasing SA of the 215 kHz-Guided frequency-path pair persists after venting. The SA and TOFS curves for the 1 MHz-Through path and 215 kHz-Guided path for each 50°C increment test are plotted together in Fig. 5. For these aggregate plots,  $\overline{SA}$  is plotted, which allows for the direct comparison of SA trends across tests on the same scale. Non-normalized SA can vary from test to test based on factors such as variation in transducer geometry or transducer adhesion to the cells.

Additionally, the occurrence and type of failure is tabulated for each hold temperature in Table 2. It can be observed in Fig. 5 that largest rate of decrease in SA occurs during the 450°C test at 10 min. This is most likely due to the rapid and highly localized damage evolution for this test. As the hold temperature is decreased, damage evolution is allowed to accumulate more gradually and heat conduction within the cell allows for thermal damage to propagate closer to the transmission path. A more gradual decrease in SA is observed for the 400°C, 350°C, and 300°C hold temperatures. For the 250°C and 200°C data the SA remains close to the initial value for a longer duration before decreasing and even increases in the 200°C case. This is most likely due to the effect of increasing pressure, which may be compressing layers and decreasing attenuation due to impedance discontinuities between layers, counteracting with SA reductions resulting from thermal damage. We hypothesize the following: as temperature propagates within the cell with increasing test time, the decrease in SA due to thermal damage outweighs the SA-increasing contribution from increasing pressure, and therefore the overall SA decreases with increasing test time.

The TOFS data in Fig. 5 displays interesting behavior indicating different regimes of damage depending on the set temperature and test time. We note that a positive TOFS may be due to several different factors. Factors include an increase in path length (i.e. an expanded cell), a reduction in the effective stiffness, a decrease in the overall mass density, or some combination of those changes. Since the cells are mechanically confined in a clamping apparatus that is much stiffer than the LIB cell, the increase in path length is negligible. Prior to venting, no change in the overall mass occurs, so cell density will be unchanged. Therefore, we attribute increases in TOF to a reduction in the effective elastic modulus due to heating. Given a constant density and thickness, the US TOF depends on the reciprocal of the square root of the stiffness, i.e. the square root of the compliance. For the case of the through-thickness path, the TOFS is given by the

$$\text{TOFS}(t) = c_0 H \left( \sqrt{C_{33,0}/C_{33}(t)} - 1 \right) \quad (3)$$

where  $H$  is the thickness of the cell,  $c_0$  is the sound speed in the thickness direction when the heating begins, i.e.  $t = 0$ ,  $C_{33}(t)$  is the instantaneous plane-wave stiffness in the thickness-direction, and  $C_{33,0} = C_{33}(t = 0)$ .

The observed positive TOFS is a nonlinear function of time, with a nonlinear change in TOFS for early test times which is clearly observed in the inset of Fig. 5(b) followed by a quasi-linear time dependence. The transition from a nonlinear to a quasi-linear function of time is most readily observable in the 200°C data, where the linear portion has a smaller slope and extends from approximately 5 min into the test until nearly 35 min. The nature of the nonlinearity in the data is unclear as we can fit a quadratic, cubic, or quartic polynomial to the nonlinear portion with coefficients of determination of .9966, .9994, and .9996 respectively. Popp et al. reported a cubic relationship between TOFS and temperature from 5°C and 45°C [6]. Although they used different cell geometry and excitation frequency, it is interesting that a nonlinear function of TOFS with temperature is also found, indicating that the same thermo-mechanical mechanisms are likely responsible for small

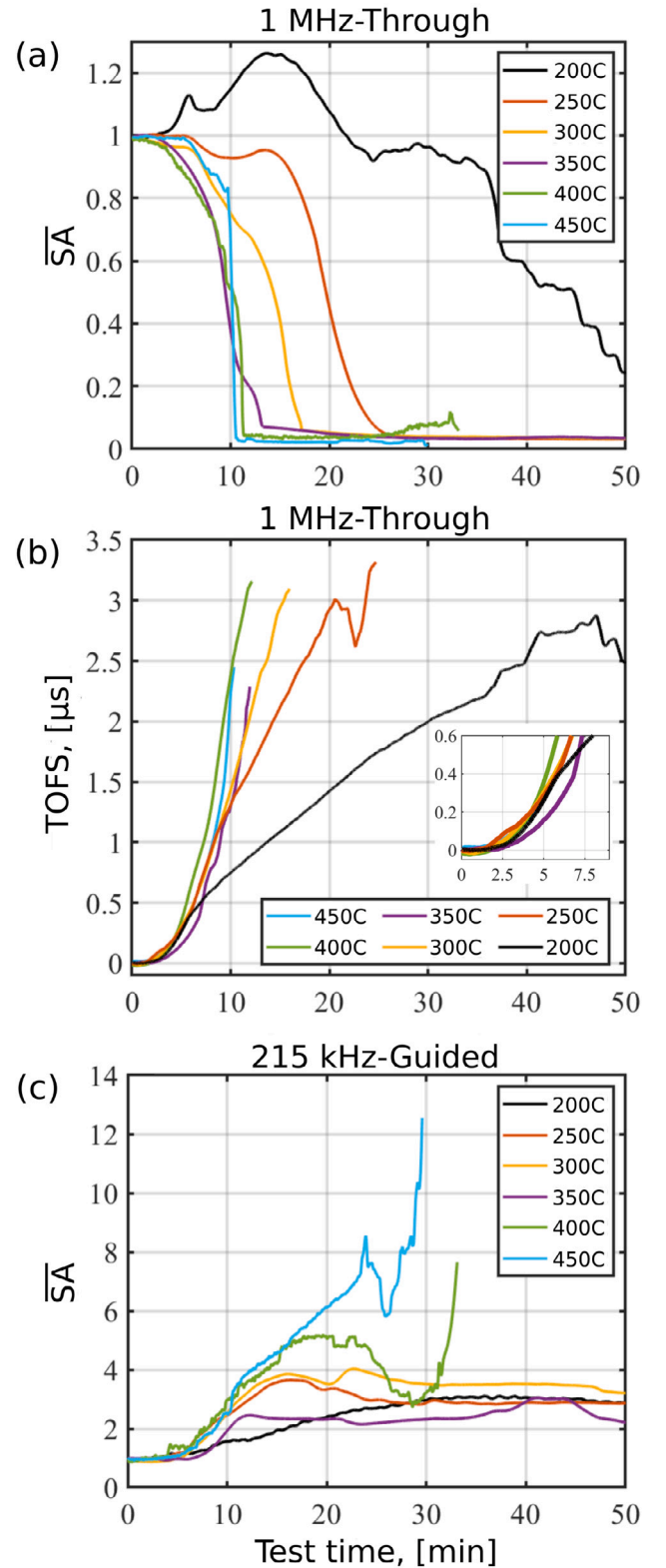


Fig. 5. US metrics plotted for each 50°C test, where data is shown up to TR (a)  $\overline{SA}$  versus time, 1 MHz-Through frequency-path pair (b) TOFS versus time, 1 MHz-Through frequency-path pair (c)  $\overline{SA}$  versus time, 215 kHz-Guided frequency-path pair.

changes in temperature in the data reported here and in that prior work. Although we cannot prescribe the functional dependence of the nonlinearity based on this data alone, we note that the nonlinear and

**Table 2**

Occurrence and type of failure observed for different test Hold temperatures.

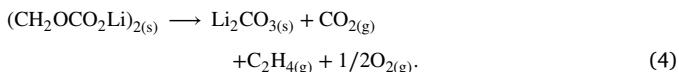
Hold temp °C	Venting	Thermal runaway
200	No	No
250	Yes	No
300	Yes	No
350	Yes	No
400	Yes	Yes
450	Yes	Yes

linear regimes of TOFS prior to TR are repeatable for different hold temperatures. Further, the nonlinear time-dependence of TOFS during early stages of thermal loading in particular may provide insight into underlying damage mechanisms that may enable early indications of thermal abuse and is therefore of interest for future investigation.

The SA data for the 215 kHz-Guided wave path for each 50°C increment test are plotted together in Fig. 5. The cells went into thermal runaway for 400°C and 450°C hold temperatures. The SA curves for the 215 kHz-Guided wave path for these two hold temperatures show the greatest increase in SA and are the only curves that do not plateau once the SA increases 2–4.5 times the value at  $t = 0$ . These curves are feature-rich and may correspond to a number of internal mechanisms including SEI decomposition, layer softening, or inter-layer delamination.

### 3.1. Detailed process of thermal runaway

Prior to discussing SA and TOFS trends, it is worthwhile to document the thermal runaway process, specifically how each component degrades, at what temperature, and how the degradation contributes to both TR and changes in mechanical properties that affect US propagation. Though the following reactions occur at all SOC, the overall reactivity and propensity for TR is increased with higher SOC [42]. With applied heat, the electrolyte partially evaporates in a state of vapor liquid equilibrium [43]. Electrolyte evaporation is the cause of initial pressure generation, and will occur whether or not the cell enters TR. The SEI is widely considered to be the first component which exothermically degrades and contributes to the onset of TR [44–46]. The SEI is composed of many different compounds and the exact SEI composition will depend on the specific components used for the electrolyte solvent, electrolyte additive solutes, and components of the anode. As such, a range of temperatures are reported for the decomposition of SEI from as low as 60°C to as high as 120°C [47–49]. The  $(\text{CH}_2\text{OCO}_2\text{Li})_2$  component of the SEI is present in all batteries which use ethyl carbonate (EC) in the electrolyte [47]. The decomposition of  $(\text{CH}_2\text{OCO}_2\text{Li})_2$  is given by the following reaction:



Importantly, the decomposition of the SEI is accompanied by heat and gas generation, which will increase the cell pressure as long as the outer cell casing remains intact. After SEI decomposition the electrolyte will react with the unprotected lithium-intercalated graphite anode. The decomposition of the  $\text{LiPF}_6$  salts present in the electrolyte occur around 110°C, at similar temperatures as SEI decomposition, and produce  $\text{PF}_5$  gas [50]. At 120°C the PVDF binder has been found to melt and possibly dissolve into the electrolyte fluid [51]. This phenomena is not widely reported in the literature as it is not a large contributor to TR, but it is worth noting in this study as the mechanical properties of the binder will change as it melts, which may in turn affect the US signal trends. At higher temperatures the separator will begin to soften and then melt, which increases the risk of internal short circuit. The most common separator materials are polyethylene (PE) and polypropylene (PP) which begin to melt at 130°C and 160°C, respectively [52].

The final reaction in thermal runaway is the decomposition of the cathode material. Cathode decomposition produces combustible oxygen gas which reacts with the electrolyte at elevated temperature. Li-ion cathodes with NMC(532) stoichiometry were found to decompose starting at 183°C [53].

While this summary comprises the chemical degradation of battery components with temperature, mechanical deformation must also be considered by looking at the mesoscopic structure of a pouch cell. The cell is composed of layers of alternating anode-separator-cathode which are all soaked in electrolyte and packed together. When a layered structure is heated the differences in thermal expansion coefficients of each layer will cause stress localization due to differences in deformation in each constituent material. In a pouch cell, these stresses can contribute to delamination between layers, which is when layers lose contact, in addition to gas generation, which is discussed below.

The gas generation of the SEI decomposition reaction helps to explain the decrease in SA for the 1 MHz-Through data, and may also help explain the sudden decreases in SA apparent in each iteration of the experiment. Since the ultrasonic wave propagating along the 1 MHz-Through path depends on a local material average within the transmission path, the occurrence of even very small gas bubbles will immediately decrease the signal amplitude due to the large impedance mismatch between solids and gases [54,55]. Additionally, the softening of the PP separator and melting of the PVDF binder partially explains the increasing TOFS for the 1 MHz-Through path data. Further, the creation of gas bubbles and subsequent delamination of layers of the cell helps provide a hypothesis for why the 215 kHz-Guided wave SA increases with thermal loading. While delamination will only decrease the SA for the 1 MHz-Through path via attenuation or reflection of propagating waves, it may increase the SA of the 215 kHz-Guided path by creating an effectively thinner elastic waveguide for the Lamb mode, thereby reducing volumetric attenuation. Full delamination between layers may be unlikely given the confinement within the pressure-rig; however, even a small amount of delamination reduces the propagation volume, by effectively changing the location of the lower boundary. Given the complexity of the guided wave model and its dependence on internal structure, specifically the depth of any delaminations which may vary between tests, the increasing SA for the 215 kHz-Guided path is not fully understood. Future work should focus on correlating changes in ultrasonic signals with other imaging techniques to better understand how one may infer the evolution of damage from changes in guided wave amplitude. Regardless, for all tests we observe increasing SA of the 215 kHz-Guided wave signal long after the signal from the 1 MHz-Through path is lost in the noise floor, including after cell venting. Notably, the higher the temperature of the localized heating, the more rapid the rise in guided wave SA, suggesting that damage such as gas formation due to SEI decomposition may be one source of SA increase, in direct contrast to through-thickness transmission mode monitoring. The SA increase is ultimately followed by a reduction in SA as the cell nears failure.

### 3.2. Establishing safety metrics

The consistent trends with heating for the SA and TOFS for the 1 MHz-Through and 215 kHz-Guided frequency-path pairs allows us to propose safety metrics to warn of an impending thermal runaway event. Metrics can be established based on TOFS increase and SA decrease for the 1 MHz-Through data. Given the fact that the TOFS is unreliable for the 215 kHz-Guided wave data in the present source-receiver configuration, only the SA data will be used to establish US metrics for this frequency-path pair. The SA metrics employ a decrease or increase of 25% and 50% for the 1 MHz-Through and 215 kHz-Guided frequency-path pairs, respectively. For the TOFS metric an increase of 2.5  $\mu\text{s}$  and 5.0  $\mu\text{s}$  are chosen for the 1 MHz-Through frequency-path pair. Each metric is reached at a certain time before the cell first ruptures. Fig. 6 shows the time before first rupture plotted against the



**Table 3**

Ultrasonic safety metrics based on SA Decrease for the 1 MHz-Through frequency-path pair.

Hold temp (°C)	SA Decrease %	Time before first rupture (min.)	Avg. cell temp (°C)	Pressure (kPa)	TR
200	25	N/A	–	–	No
200	50	N/A	–	–	No
250	25	12.1	122.6	71.6	No
250	50	10.6	124.6	77.2	No
300	25	11.0	118.9	47.0	No
300	50	6.8	134.0	76.4	No
350	25	10.5	82.3	46.7	No
350	50	9.0	104.5	49.5	No
400	25	3.1	146.0	101.3	Yes
400	50	0.7	162.8	177.6	Yes
450	25	0.7	141.4	68.5	Yes
450	50	0.5	147.9	74.4	Yes

hold temperature for each metric. The worst-case scenario for these metrics is for the 1 MHz-Through SA metric for a hold temperature of 450°C. In this scenario, the ultrasonic metric gives warning of only 0.7 min before rupture. However, the 450°C indicators for 1 MHz-Through TOFS and 215 kHz-Guided SA give warnings of 5.8 min and 5.0 min before rupture, respectively. It is important to note that these are warnings in advance of cell rupture not TR, so in practice the user would have more time than this to avoid a more dangerous failure. The greatest advanced warnings provided by the 1 MHz-Through SA, 215 kHz-Guided SA, and 1 MHz-Through TOFS metrics are 12.1 min, 24.2 min, and 25.4 min, respectively. To add context to these metric values, we also report the average cell temperature and cell pressure when each metric is reached in Tables 3, 4, and 5. Importantly, for the 2.5  $\mu$ s TOFS and the 25% increase in 215 kHz-Guided SA metrics, the highest average cell temperature for any 50 °C increment test is 75.2 °C and 85.6 °C, respectively. While these average cell temperatures are above the reported limit for this cell, our average cell temperature measurement is the average of all four thermocouples. In practice it is unlikely to have a thermocouple directly at the heat source, and given the very large difference in temperature at each thermocouple location due to the low thermal conductivity of the cell, as indicated by the representative case shown in Fig. 4, if we instead average the three thermocouples not including the thermocouple at the heat source, the average cell temperature at these metrics is 27.1 °C and 30.0 °C, respectively. Temperature measurements are therefore only reliable in practice when heating is uniform and localized heating is highly likely to go undetected unless a thermocouple is co-located with the heating source. Additionally, the highest pressure at the 2.5  $\mu$ s TOFS and the 25% increase in 215 kHz-Guided SA metrics is 48.2 kPa and 47.7 kPa, respectively. These pressures are not unexpected in practice, as the volume change due to normal cycling can induce pressure increases as high as 9.37 times [34]. It is also worth mentioning that while previous work has suggested that SA data is less reliable than TOFS data, any claim about SA trend should be qualified with the frequency and wave-type being excited. While it is true that a high-frequency, collimated beam is more sensitive to damage evolution within the transmission path and that this damage evolution is stochastic in nature, in this work the SA trend data for both the 215 kHz-Guided and 1 MHz-Through frequency-path pairs provides consistent indicators of cell damage and could be used together to provide a more reliable indication of damage associated with thermal abuse.

#### 4. Conclusion

In this work, two frequency-path pairs were used to investigate the applicability of ultrasonic inspection to detect thermal abuse in lithium-ion batteries in advance of traditional monitoring methods. Further, by investigating localized heating, we have expanded the applicability

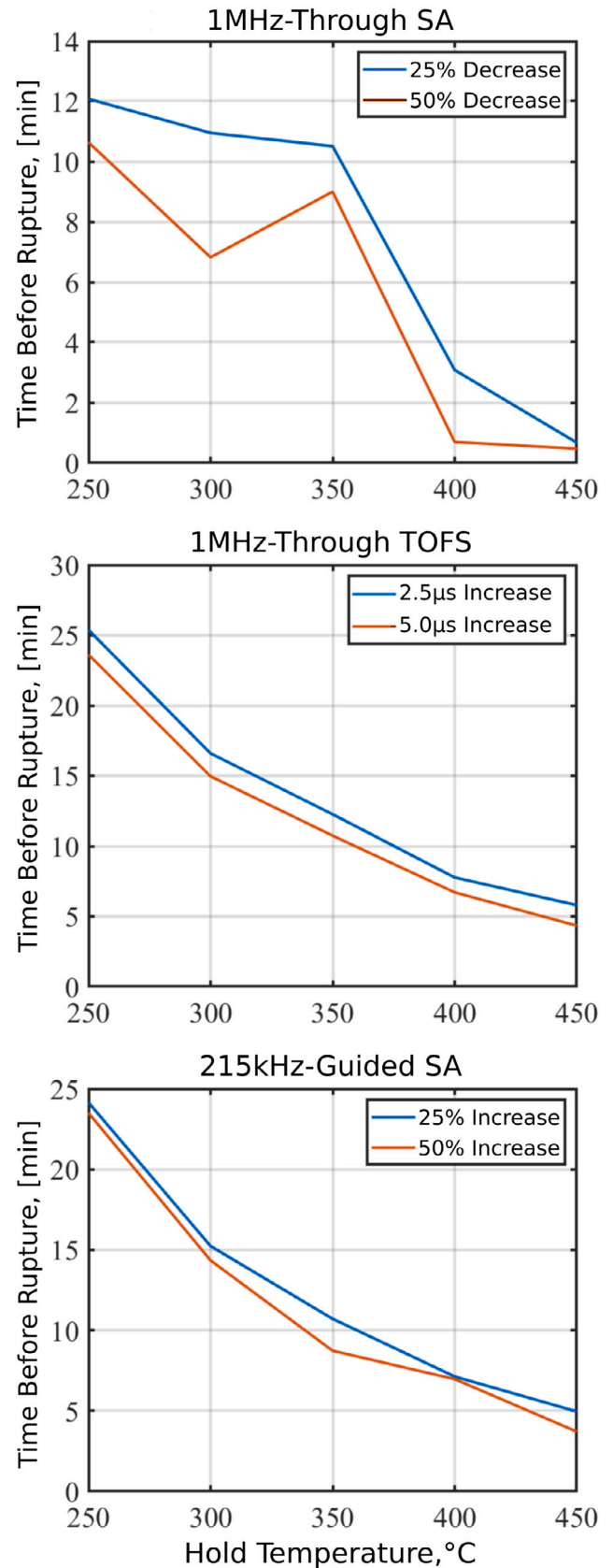


Fig. 6. Time before first rupture indicated by SA and TOFS metrics as a function of localized hold temperature.



**Table 4**

Ultrasonic safety metrics based on SA Increase for the 215 kHz-Guided frequency-path pair.

Hold temp (°C)	SA Increase %	Time before first rupture (min.)	Avg. cell temp (°C)	Pressure (kPa)	TR
200	25	N/A	–	–	No
200	50	N/A	–	–	No
250	25	24.2	81.1	47.7	No
250	50	23.5	85.1	48.2	No
300	25	15.2	85.6	40.0	No
300	50	14.3	96.5	39.9	No
350	25	10.7	84.2	47.2	No
350	50	8.7	105.6	50.3	No
400	25	7.1	82.9	44.9	Yes
400	50	7.0	85.1	45.4	Yes
450	25	5.0	78.4	39.9	Yes
450	50	3.7	103.1	41.4	Yes

**Table 5**

Ultrasonic safety metrics based on TOFS for the 1 MHz-Through frequency-path pair.

Hold temp (°C)	TOF Shift (μs)	Time before first rupture (min.)	Avg. cell temp (°C)	Pressure (kPa)	TR
200	2.5	N/A	–	–	No
200	5.0	N/A	–	–	No
250	2.5	25.4	58.0	47.9	No
250	5.0	23.6	79.6	47.3	No
300	2.5	16.6	60.8	40.6	No
300	5.0	15.0	83.0	39.3	No
350	2.5	12.3	64.7	48.2	No
350	5.0	10.7	83.9	47.4	No
400	2.5	7.8	75.2	44.1	Yes
400	5.0	6.7	91.3	46.2	Yes
450	2.5	5.8	68.5	42.1	Yes
450	5.0	4.3	90.5	40.4	Yes

of US damage detection by showing that transducer location does not need to be co-located with the heat source to enable the detection of damage due to thermal abuse. Repeatable and consistent SA and TOFS trends were observed as pouch cells were subjected to localized heating. Specifically, the SA decreases and TOFS increases for the 1 MHz-Through frequency-path pair, while the SA increases for the 215 kHz-Guided wave frequency-path pair. A finite element model was constructed using transversely isotropic material properties found using a homogenization model of the layered LIB to visualize how the acoustic energy propagates within the pouch cell. It was found that the 215 kHz excitation excites a Lamb-like mode that is influenced by the geometry of the cell including the top and bottom surfaces. It was also found that the 1 MHz excitation generates a collimated beam that travels directly from the transmitting transducer to the receiving transducer on the opposite side of the cell. With this understanding of the wave propagation within the cell, the SA and TOFS trends for the 1 MHz-Through frequency-path pair were hypothesized to be due to the softening of the PP separator which would decrease the speed of sound of the cell while also increasing the attenuation. The SA trend for the 215 kHz-Guided frequency-path pair is more difficult to interpret, but may be attributed to a relative thinning of the medium as delamination and gas formation forces layers apart. From the SA and TOFS data, we derived metrics to provide a real-time warning of an impending TR event. The SA and TOFS metrics all provided advanced warning before cell venting, at worst providing 0.67 min and at best providing 25.4 min before venting, which occurs many minutes before TR. This work has demonstrated the viability of using different frequencies to selectively excite different propagation modes to create valuable metrics to warn of impending TR well in advance of catastrophic failure.

## CRediT authorship contribution statement

**Tyler M. McGee:** Writing – original draft, Investigation, Formal analysis, Methodology, Software, Data curation, Visualization. **Barrett Neath:** Writing – original draft, Investigation, Formal analysis, Methodology, Software, Data curation, Visualization. **Sam Matthews:** Methodology, Resources, Writing – review & editing. **Ofodike A. Ezekoye:** Conceptualization, Writing – review & editing, Funding acquisition, Project administration, Supervision. **Michael R. Haberman:** Conceptualization, Writing – review & editing, Funding acquisition, Project administration, Supervision.

## Declaration of competing interest

The authors declare that they have no known competing financial interests or personal relationships that could have appeared to influence the work reported in this paper.

## Data availability

Data will be made available on request.

## Acknowledgment

T. M., S. M., O. A. E., and M. R. H. acknowledge partial support from General Motors and B. N. was supported by the Applied Research Laboratories Chester M. McKinney Graduate Fellowship in Acoustics.

## Appendix

### A.1. Elastic homogenization model for layered Li-ion pouch cells

To approximate the effective transversely isotropic material properties of layered LIB pouch cells in the long-wavelength limit, we present a simple homogenization model based on a unit cell consisting of a layering scheme of a separator, an anode, another separator, and a cathode in that order, as illustrated in Fig. 7. Dividing each individual layer thickness by the total thickness of the unit cell gives length fractions for each of the constituent materials. The effective density of the unit cell, and thus the entire pouch cell, is simply the Archimedean (or volumetric) average which can be found by multiplying the density of each component by its length fraction according to Eq. (5),

$$\rho^e = \phi_a \rho_a + \phi_c \rho_c + \phi_s \rho_s. \quad (5)$$

The stiffness tensor of the layered cell can be modeled as a transversely isotropic medium. This means the material properties are isotropic in the  $x_1 - x_2$  plane, but are different in the thickness direction,  $x_3$ . The stiffness tensor for transversely isotropic media has five independent constants:  $C_{11}$ ,  $C_{13}$ ,  $C_{33}$ ,  $C_{44}$ , and  $C_{66}$  [40]. Constants  $C_{11}$  and  $C_{33}$  are the elastic moduli relating stress and strain for plane waves propagating along in-plane and through-thickness directions, respectively, constants  $C_{44}$  and  $C_{66}$  are the shear moduli for angular deformation in the  $x_1 - x_3$  and  $x_1 - x_2$  planes, respectively, and  $C_{13} = C_{31}$  provides information about stresses generated due to the Poisson-effect. For a transversely isotropic material  $C_{12} = C_{11} - 2C_{66}$ .

For in-plane deformations, we can make the simplifying assumption that all constituent materials undergo the same deformation along  $x_1$ . This is the well-known Voigt average [39]. By taking the Voigt average of the  $C_{11}$  plane-wave modulus of each constituent material given in Table A.6, the effective modulus is calculated using Eq. (6), which is analogous to Eq. (5) for the mass density. Note that  $C_{22} = C_{11}$  for transversely isotropic media with the geometry shown in Fig. 7.

$$C_{11}^e = \phi_a C_{11,a} + \phi_c C_{11,c} + \phi_s C_{11,s} \quad (6)$$

**Table A.6**  
Stiffness tensor elements of the anode, cathode, and separator.

Material	$C_{11}$ GPa	$C_{12}$ GPa	$C_{13}$ GPa	$C_{22}$ GPa	$C_{23}$ GPa	$C_{33}$ GPa	$C_{44}$ GPa	$C_{55}$ GPa	$C_{66}$ GPa	$\nu$	Density kg/m <sup>3</sup>
CoO <sub>2</sub> [36]	264	163	7.6	264	163	13.5	5.1	5.1	5.1	.32	1540
LiC <sub>6</sub> [36]	989	171	2.1	989	171	78.0	21.9	21.9	409	.24	1060
PP [37]	2.83	1.49	1.49	2.83	1.49	2.83	.668	.668	.668	.49	900

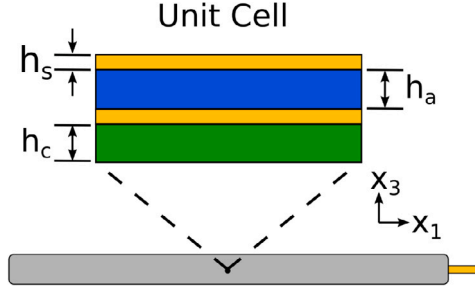


Fig. 7. Simplified three-component unit cell of a pouch cell battery.

Subscripts a, c, and s refer to the stiffness tensor values corresponding to the anode, cathode, or separator respectively. This model assumes the polypropylene separator to be isotropic. Measuring stiffness tensor components of the as-built battery components is an area of active research.

The effective plane-wave stiffness in the thickness direction,  $C_{33}$ , is calculated by assuming that the stress is uniform in each constituent material of the unit cell. This is the well-known Reuss, or harmonic, average [39], which is given by the relation

$$C_{33}^{\text{eff}} = [\phi_a/C_{33,a} + \phi_c/C_{33,c} + \phi_s/C_{33,s}]^{-1}. \quad (7)$$

Given the geometry of the unit cell, we use a similar approach to determine the shear moduli in the  $x_1-x_2$ - and  $x_1-x_3$ -planes. We assume that angular deformation in the  $x_1-x_2$ -plane is the same for all layers, and therefore we can approximate the  $C_{66}$  component of the stiffness tensor using a Voigt average in the same way as Eq. (6), replacing the  $C_{11}$  modulus of each component with their respective shear modulus. For shearing in the  $x_1-x_3$ -plane, we assume that each constituent material is subjected to the same shear stress. We therefore use the Reuss average to estimate the  $C_{44}$  component of the stiffness tensor using Eq. (7) with the shear moduli of each component replacing its respective plane-wave modulus,  $C_{33}$ .

The final tensor component to be calculated is the  $C_{13}$  component. We can relate the  $C_{13}$  component to the  $C_{33}$  by assuming that the stress in each component in the  $x_3$  direction and the strain in each component in the  $x_2$  direction are both zero. This reduces the stress-strain relationships such that the  $C_{13}$  component is related to the  $C_{33}$  component by the Poisson's ratio,  $\nu_{13}$ . The effective Poisson's ratio can be calculated using a Voigt average in the same way as Eq. (6), replacing the  $C_{11}$  modulus of each component with their respective Poisson's ratio. This yields the relation for  $C_{13}$  is given by Eq. (8),

$$C_{13}^e = \nu^e C_{33}^e. \quad (8)$$

## A.2. COMSOL model details

To visualize and understand the wave propagation within the cell a model is created using COMSOL Multiphysics 5.6. A full 3D time-domain model is used with both the Electrostatics and Solid Mechanics Physics packages. The effective stiffness tensor values calculated in the previous section are used to define a custom material in COMSOL that represents the pouch cell as a single homogeneous medium with a

transversely isotropic stiffness. The cell geometry including the transducers is modeled exactly as the cells exist in practice. The material assigned to the transducers is PZT-4 with polarization along the  $x_3$ -axis. Electrostatic boundary conditions are assigned to the transducers. For each transducer the face which coincides with the pouch cell is given a Ground boundary condition. The top surfaces of all receiving transducers are assigned Floating Potentials so that the received signals on each transducer can be observed. The transducers are defined within the Solid Mechanics Physics as Piezoelectric Materials. Within the Multiphysics the Piezoelectric Effect is applied to each transducer. For the transmitting transducer the top surface is assigned a time-varying Electric Potential. To simulate the Gaussian-modulated cosine input an analytic expression is created according to the following Eq. (9),

$$V(t) = V_0 \cos(\omega_0(t - t_0)) \exp\left(-\frac{(t - t_0)^2}{2T^2}\right). \quad (9)$$

The argument of Eq. (9) is the variable  $t$ . Every other variable is defined within the Parameters section. The variable  $t_0$  represents the time of the maximum applied voltage for the Gaussian-modulated signal relative to  $t = 0$ . The variable  $T$  defines the width of the Gaussian-modulated signal envelope and  $V_0$  defines the amplitude of applied voltage for the Gaussian-modulated excitation signal. Finally,  $\omega_0$  defines the center frequency, in rad/s, of the Gaussian-modulated pulse, with  $\omega_0 = 2\pi f_0$ , where  $f_0$  is the center frequency in Hz. After defining all materials, boundary conditions, analytic expressions, and parameters the Study is begun. A Time Dependent study is run with a time range from 0–50  $\mu\text{s}$  with a step-size of 0.1  $\mu\text{s}$ .

## References

- [1] M.A. Hannan, M.H. Lipu, A. Hussain, A. Mohamed, A review of lithium-ion battery state of charge estimation and management system in electric vehicle applications: Challenges and recommendations, *Renew. Sustain. Energy Rev.* 78 (2017) 834–854, <http://dx.doi.org/10.1016/j.rser.2017.05.001>.
- [2] G. Xia, L. Cao, G. Bi, A review on battery thermal management in electric vehicle application, *J. Power Sources* 367 (2017) 90–105, <http://dx.doi.org/10.1016/j.jpowsour.2017.09.046>.
- [3] B. Sood, M. Osterman, M. Pecht, Health monitoring of lithium-ion batteries, in: 2013 IEEE Symposium on Product Compliance Engineering, ISPC, 2013, pp. 1–6, <http://dx.doi.org/10.1109/ISPC.2013.6664165>.
- [4] Q. Ke, S. Jiang, W. Li, W. Lin, X. Li, H. Huang, Potential of ultrasonic time-of-flight and amplitude as the measurement for state of charge and physical changes of lithium-ion batteries, *J. Power Sources* 549 (2022) 232031, <http://dx.doi.org/10.1016/j.jpowsour.2022.232031>.
- [5] R.E. Owen, J.B. Robinson, J.S. Weaving, M.T. Pham, T.G. Tranter, T.P. Neville, D. Billson, M. Braglia, R. Stocker, A.A. Tidblad, et al., Operando ultrasonic monitoring of lithium-ion battery temperature and behaviour at different cycling rates and under drive cycle conditions, *J. Electrochem. Soc.* 169 (4) (2022) 040563, <http://dx.doi.org/10.1149/1945-7111/ac6833>.
- [6] H. Popp, M. Koller, S. Keller, G. Glanz, R. Klambauer, A. Bergmann, State estimation approach of lithium-ion batteries by simplified ultrasonic time-of-flight measurement, *IEEE Access* (2019) <http://dx.doi.org/10.1109/ACCESS.2019.2955556>.
- [7] D. Rohrbach, E. Garcia-Tamayo, J. Potter, V. Martinez, M. Bernal, Nondestructive state-of-charge assessment of Lithium-ion batteries using quantitative ultrasound spectroscopy, in: 2021 IEEE International Ultrasonics Symposium, IUS, 2021, pp. 1–4, <http://dx.doi.org/10.1109/IUS52206.2021.9593566>.
- [8] G. Zhao, Y. Liu, G. Liu, S. Jiang, W. Hao, State-of-charge and state-of-health estimation for lithium-ion battery using the direct wave signals of guided wave, *J. Energy Storage* 39 (2021) <http://dx.doi.org/10.1016/j.est.2021.102657>.

- [9] P. Ladpli, F. Kopsaftopoulos, F.-K. Chang, Estimating state of charge and health of lithium-ion batteries with guided waves using built-in piezoelectric sensors/actuators, *J. Power Sources* 384 (2018) 342–354, <http://dx.doi.org/10.1016/j.jpowsour.2018.02.056>.
- [10] R.J. Copley, D. Cumming, Y. Wu, R.S. Dwyer-Joyce, Measurements and modelling of the response of an ultrasonic pulse to a lithium-ion battery as a precursor for state of charge estimation, *J. Energy Storage* 36 (2021) <http://dx.doi.org/10.1016/j.est.2021.102406>.
- [11] J.B. Robinson, M. Maier, G. Alster, T. Compton, D.J. Brett, P.R. Shearing, Spatially resolved ultrasound diagnostics of Li-ion battery electrodes, *Phys. Chem. Chem. Phys.* 21 (12) (2019) 6354–6361, <http://dx.doi.org/10.1039/c8cp07098a>.
- [12] L. Gold, T. Bach, W. Virsik, A. Schmitt, J. Müller, T.E.M. Staab, G. Sextl, Probing lithium-ion batteries' state-of-charge using ultrasonic transmission – Concept and laboratory testing, *J. Power Sources* 343 (2017) 536–544, <http://dx.doi.org/10.1016/j.jpowsour.2017.01.090>.
- [13] G. Davies, K.W. Knehr, B. Van Tassell, T. Hodson, S. Biswas, A.G. Hsieh, D.A. Steingart, State of charge and state of health estimation using electrochemical acoustic time of flight analysis, *J. Electrochem. Soc.* 164 (12) (2017) A2746–A2755, <http://dx.doi.org/10.1149/2.1411712jes>.
- [14] A.G. Hsieh, S. Bhadra, B.J. Hertzberg, P.J. Gjeltema, A. Goy, J.W. Fleischer, D.A. Steingart, Electrochemical-acoustic time of flight: In operando correlation of physical dynamics with battery charge and health, *Energy Environ. Sci.* 8 (5) (2015) 1569–1577, <http://dx.doi.org/10.1039/C5EE00111K>.
- [15] R. Schmidt, J. Sakamoto, In-situ, non-destructive acoustic characterization of solid state electrolyte cells, *J. Power Sources* 324 (2016) <http://dx.doi.org/10.1016/j.jpowsour.2016.05.062>.
- [16] C. Bommier, W. Chang, J. Li, S. Biswas, G. Davies, J. Nanda, D. Steingart, Operando acoustic monitoring of SEI formation and long-term cycling in NMC/SiGr composite pouch cells, *J. Electrochem. Soc.* 167 (2020) <http://dx.doi.org/10.1149/1945-7111/ab68d6>.
- [17] L. Oca, N. Guillet, R. Tessard, U. Iraola, Lithium-ion capacitor safety assessment under electrical abuse tests based on ultrasound characterization and cell opening, *J. Energy Storage* 29 (2019) <http://dx.doi.org/10.1016/j.est.2019.02.033>.
- [18] M. Musiak, Z. Li, Real time ultrasonic monitoring of solid-state lithium-ion cells in the frequency domain, in: 2021 IEEE International Conference on Prognostics and Health Management, 2021, <http://dx.doi.org/10.1109/ICPHM51084.2021.9486632>.
- [19] C. Bommier, W. Chang, Y. Lu, J. Yeung, G. Davies, R. Mohr, M. Williams, D. Steingart, In operando acoustic detection of lithium metal plating in commercial LiCoO<sub>2</sub>/Graphite pouch cells, *Cell Rep. Phys. Sci.* 1 (2020) <http://dx.doi.org/10.1016/j.scrp.2020.100035>.
- [20] W. Chang, D. Steingart, Operando 2D acoustic characterization of lithium-ion battery spatial dynamics, *ACS Energy Lett.* (2021) <http://dx.doi.org/10.1109/acsenergylett.1c01324>.
- [21] W. Chang, C. Bommier, T. Fair, J. Yeung, S. Patil, D. Steingart, Understanding adverse effects of temperature shifts on Li-ion batteries: An operando acoustic study, *J. Electrochem. Soc.* 167 (9) (2020) <http://dx.doi.org/10.1149/1945-7111/ab6c56>.
- [22] Y. Wu, Y. Wang, W.K.C. Yung, M. Pecht, Ultrasonic health monitoring of lithium-ion batteries, *Electronics* 8 (7) (2019) <http://dx.doi.org/10.3390/electronics8070751>.
- [23] M.T. Pham, J.J. Darst, D.P. Finegan, J.B. Robinson, T.M. Heenan, M.D. Kok, F. Iacoviello, R. Owen, W.Q. Walker, O.V. Magdysyuk, T. Connolly, E. Darcy, G. Hinds, D.J. Brett, P.R. Shearing, Correlative acoustic time-of-flight spectroscopy and X-ray imaging to investigate gas-induced delamination in lithium-ion pouch cells during thermal runaway, *J. Power Sources* 470 (2020) <http://dx.doi.org/10.1016/j.jpowsour.2020.228039>.
- [24] M.C. Appleberry, J.A. Kowalski, S.A. Africk, J. Mitchell, T.C. Ferree, V. Chang, V. Parekh, Z. Xu, Z. Ye, J.F. Whitacre, et al., Avoiding thermal runaway in lithium-ion batteries using ultrasound detection of early failure mechanisms, *J. Power Sources* 535 (2022) 231423, <http://dx.doi.org/10.1016/j.jpowsour.2022.231423>.
- [25] H. Zappen, G. Fuchs, A. Gitis, D.U. Sauer, In-operando impedance spectroscopy and ultrasonic measurements during high-temperature abuse experiments on lithium-ion batteries, *Batteries* 6 (2) (2020) <http://dx.doi.org/10.3390/batteries6020025>.
- [26] A. Kirchev, N. Guillet, L. Lonardoni, S. Dumenil, V. Gau, Li-ion cell safety monitoring using mechanical parameters: Part II. battery behavior during thermal abuse tests, *J. Electrochem. Soc.* (2022) <http://dx.doi.org/10.1149/1945-7111/acada6>.
- [27] Z. Li, J. Zhang, B. Wu, J. Huang, Z. Nie, Y. Sun, F. An, N. Wu, Examining temporal and spatial variations of internal temperature in large-format laminated battery with embedded thermocouples, *J. Power Sources* 241 (2013) 536–553, <http://dx.doi.org/10.1016/j.jpowsour.2013.04.117>.
- [28] J. Yi, U.S. Kim, C.B. Shin, T. Han, S. Park, Three-dimensional thermal modeling of a lithium-ion battery considering the combined effects of the electrical and thermal contact resistances between current collecting tab and lead wire, *J. Electrochem. Soc.* 160 (3) (2013) A437, <http://dx.doi.org/10.1149/2.039303jes>.
- [29] J.B. Robinson, J.A. Darr, D.S. Eastwood, G. Hinds, P.D. Lee, P.R. Shearing, O.O. Taiwo, D.J. Brett, Non-uniform temperature distribution in li-ion batteries during discharge—A combined thermal imaging, X-ray micro-tomography and electrochemical impedance approach, *J. Power Sources* 252 (2014) 51–57, <http://dx.doi.org/10.1016/j.jpowsour.2013.11.059>.
- [30] D.J. Noelle, M. Wang, A.V. Le, Y. Shi, Y. Qiao, Internal resistance and polarization dynamics of lithium-ion batteries upon internal shorting, *Appl. Energy* 212 (2018) 796–808, <http://dx.doi.org/10.1016/j.apenergy.2017.12.086>.
- [31] E. Archibald, R. Kennedy, K. Marr, J. Jeevarajan, O. Ezekoye, Characterization of thermally induced runaway in pouch cells for propagation, *Fire Technol.* 56 (2020) 2467–2490, <http://dx.doi.org/10.1007/s10694-020-00974-2>.
- [32] R.W. Kennedy, O.A. Ezekoye, Experimental and modeling characterization of nickel-manganese-cobalt (532) lithium ion battery arrays with thermal separators, *J. Energy Storage* 60 (2023) 106682, <http://dx.doi.org/10.1016/j.est.2023.106682>.
- [33] T. McGee, E. Archibald, O.A. Ezekoye, M.R. Haberman, Ultrasonic inspection of lithium-ion batteries to determine state of charge, state of health, and battery safety, *J. Acoust. Soc. Am.* 146 (4) (2019) 2816–2817, <http://dx.doi.org/10.1121/1.5136756>.
- [34] L. Hovestadt, K. Wildermann, A. Sahhary, R. Hanke-Rauschenbach, Investigation of temperature and pressure behavior of constrained lithium ion cell under lithium plating conditions, *J. Electrochem. Soc.* 167 (2020) <http://dx.doi.org/10.1149/1945-7111/aba550>.
- [35] J. Cannarella, C. Arnold, Stress evolution and capacity fade in constrained lithium-ion pouch cells, *J. Power Sources* 245 (2013) <http://dx.doi.org/10.1016/j.jpowsour.2013.06.165>.
- [36] Y. Qi, L.G. Hector, C. James, K.J. Kim, Lithium concentration dependent elastic properties of battery electrode materials from first principles calculations, *J. Electrochem. Soc.* 161 (11) (2014) F3010–F3018, <http://dx.doi.org/10.1149/2.0031411jes>.
- [37] D. Vgenopoulos, J. Sweeney, C. Grant, G. Thompson, P. Spencer, P. Caton-Rose, P. Coates, Nanoindentation analysis of oriented polypropylene: Influence of elastic properties in tension and compression, *Polymer* 151 (2018) <http://dx.doi.org/10.1016/j.polymer.2018.07.080>.
- [38] A. Manthiram, A reflection on lithium-ion battery cathode chemistry, *Nat. Commun.* 11 (1) (2020) 1–9, <http://dx.doi.org/10.1038/s41467-020-15355-0>.
- [39] R.M. Christensen, *Mechanics of Composite Materials*, Courier Corporation, 2012.
- [40] J.L. Rose, *Ultrasonic Guided Waves in Solid Media*, Vol. 9781107048, Cambridge University Press, 2014, p. 512, <http://dx.doi.org/10.1017/CBO9781107273610>.
- [41] G. Jie, Z. Liangheng, L. Yan, S. Fan, W. Bin, H. Cunfu, Ultrasonic guided wave measurement and modeling analysis of the state of charge for lithium-ion battery, *J. Energy Storage* 72 (2023) 108384.
- [42] H.M. Barkholtz, Y. Preger, S. Ivanov, J. Langendorf, L. Torres-Castro, J. Lamb, B. Chalamala, S.R. Ferreira, Multi-scale thermal stability study of commercial lithium-ion batteries as a function of cathode chemistry and state-of-charge, *J. Power Sources* 435 (2019) 226777, <http://dx.doi.org/10.1016/j.jpowsour.2019.226777>.
- [43] J.K. Ostanek, W. Li, P.P. Mukherjee, K. Crompton, C. Hacker, Simulating onset and evolution of thermal runaway in Li-ion cells using a coupled thermal and venting model, *Appl. Energy* 268 (2020) 114972, <http://dx.doi.org/10.1016/j.apenergy.2020.114972>.
- [44] X. Feng, M. Ouyang, X. Liu, L. Lu, Y. Xia, X. He, Thermal runaway mechanism of lithium ion battery for electric vehicles: A review, *Energy Storage Mater.* 10 (2018) <http://dx.doi.org/10.1016/j.ensm.2017.05.013>.
- [45] S. Ma, M. Jiang, P. Tao, C. Song, J. Wu, J. Wang, T. Deng, W. Shang, Temperature effect and thermal impact in lithium-ion batteries: A review, *Prog. Nat. Sci. Mater. Int.* 28 (2018) <http://dx.doi.org/10.1016/j.pnsc.2018.11.002>.
- [46] S. Bilyaz, K.C. Marr, O.A. Ezekoye, Modeling of thermal runaway propagation in a pouch cell stack, *Fire Technol.* 56 (6) (2020) 2441–2466, <http://dx.doi.org/10.1007/s10694-020-00970-6>.
- [47] A. Andersson, K. Edstrom, Chemical composition and morphology of the elevated temperature SEI on graphite, *J. Electrochem. Soc.* 148 (2001) <http://dx.doi.org/10.1149/1.1397771>.
- [48] H. Maleki, Thermal stability studies of li-ion cells and components, *J. Electrochem. Soc.* 146 (1999) <http://dx.doi.org/10.1149/1.1392458>.
- [49] D. Finegan, M. Scheel, J. Robinson, B. Tjaden, I. Hunt, T. Mason, J. Millichamp, M. Di Michiel, G. Offer, G. Hinds, D. Brett, P. Shearing, In operando high-speed tomography of lithium-ion batteries during thermal runaway, *Nature Commun.* (2015) <http://dx.doi.org/10.1038/ncomms7924>.
- [50] H. Yang, G. Zhuang, P. Ross Jr., Thermal stability of LiPF<sub>6</sub> salt and Li-ion battery electrolytes containing LiPF<sub>6</sub>, *J. Power Sources* 161 (2006) <http://dx.doi.org/10.1016/j.jpowsour.2006.03.058>.
- [51] L. Bodenes, R. Naturel, H. Martinez, R. Dedryvere, M. Menetrier, L. Croguennec, J.-P. Peres, C. Tessier, F. Fischer, Lithium secondary batteries working at very high temperature: Capacity fade and understanding of aging mechanisms, *J. Power Sources* 236 (2013) <http://dx.doi.org/10.1016/j.jpowsour.2013.02.067>.

- [52] G. Venugopal, J. Moore, J. Howard, S. Pendalwar, Characterization of micro-porous separators for lithium-ion batteries, *J. Power Sources* 77 (1999) [http://dx.doi.org/10.1016/S0378-7753\(98\)00168-2](http://dx.doi.org/10.1016/S0378-7753(98)00168-2).
- [53] J. Gong, Q. Wang, J. Sun, Thermal analysis of nickel cobalt lithium manganese with varying nickel content used for lithium ion batteries, *Thermochim. Acta* 655 (2017) <http://dx.doi.org/10.1016/j.tca.2017.06.022>.
- [54] D.E.W. Stone, B. Clarke, Ultrasonic attenuation as a measure of void content in carbon-fibre reinforced plastics, *Non-Destr. Test.* 8 (3) (1975) 137–145, [http://dx.doi.org/10.1016/0029-1021\(75\)90023-7](http://dx.doi.org/10.1016/0029-1021(75)90023-7).
- [55] H. Jeong, Effects of voids on the mechanical strength and ultrasonic attenuation of laminated composites, *J. Compos. Mater.* 31 (3) (1997) 276–292, <http://dx.doi.org/10.1177/002199839703100303>.